RSC Advances

PAPER

View Article Online
View Journal | View Issue

Cite this: *RSC Adv.*, 2025, **15**, 50521

P–N heterojunction-enhanced structural stability of tungsten disulfide nanosheets for highly efficient, stable alkaline water electrolysis

Kumasser Kusse Kuchayita, [a] Yohannes Asmare Fesseha,[a] Chih-Wei Chiu, [c] Jem-Kun Chen, [c] Ai-Wei Lee*[d] and Chih-Chia Cheng *[ab]

Tungsten disulfide (WS_2) exhibits decent electrocatalytic performance toward the hydrogen evolution reaction (HER) in acidic conditions; however, poor structural stability under alkaline conditions limits its widespread application in electrocatalysis. We developed a robust exfoliation strategy using water-soluble sodium-ion-functionalized chitosan to obtain stable, well-dispersed WS_2 nanosheets with excellent resistance to alkaline environments. Through subsequent electropolymerization and electroactivation, N-type WS_2 nanosheets were combined with P-type polyaniline on nickel foam, creating a stable organic–inorganic P–N heterojunction electrocatalytic electrode. The electrode demonstrates high HER electrocatalytic performance in 1.0 M potassium hydroxide solution, achieving a low overpotential of 24.5 mV at 10 mA cm^{-2}, a Tafel slope of 48.2 mV dec^{-1} and a low resistance of around 0.5 Ω, equivalent to the conventional noble-metal Pt/C electrocatalyst. More importantly, the electrode maintained excellent long-term electrocatalytic performance and structural integrity after 1000 cycles of cyclic voltammetry and 24 h of continuous operation at 100 mA cm^{-2}. In contrast, the catalytic activity of commercial Pt/C declined substantially, indicating poor stability under alkaline conditions. Therefore, these findings overcome the limitations of WS_2 under alkaline conditions and provide a cost-effective strategy for producing highly active, pH-universal electrocatalysts suitable for water electrolysis and sustainable hydrogen production.

Received 10th November 2025
Accepted 10th December 2025

DOI: 10.1039/d5ra08680a

rsc.li/rsc-advances

1. Introduction

The intensifying global energy crisis and ecological issues have heightened the demand for clean and sustainable energy technologies. Among the diverse approaches explored, electrocatalytic water splitting has emerged as a potential method for producing renewable hydrogen fuel by utilizing Earth's abundant water resources. Hydrogen is widely recognized as a renewable and carbon-neutral energy vector with tremendous promise for replacing fossil fuels in the future energy environment. Hydrogen is widely regarded as a renewable and carbon-neutral energy carrier that is anticipated to replace non-renewable fossil fuels in the future.[1] Green hydrogen production *via* alkaline water electrolysis, especially when powered by renewable energy sources like solar and wind, offers an environmentally friendly pathway. However, the sluggish kinetics of the hydrogen evolution reaction (HER) and oxygen evolution reaction (OER) in alkaline conditions lead to significant energy losses and thereby limit the industrial scalability of alkaline water electrolysis. Although noble metals like ruthenium (Ru), iridium (Ir), and platinum (Pt), as well as their oxides such as iridium oxide (IrO_2) and ruthenium oxide (RuO_2), exhibit excellent catalytic performance, their high cost, limited stability, and scarcity hinder the practical application of these materials.[1,2] The HER is particularly challenging in alkaline media because it requires an additional water dissociation step to generate protons, which slows down the reaction rate compared to acidic conditions. Even the benchmark HER catalyst, Pt, exhibits significantly reduced activity under alkaline conditions,[3,4] primarily due to a slow water dissociation rate, altered hydrogen bonding interactions, and changes in water adsorption characteristics.[5–7] Therefore, to address the growing demand for sustainable energy, there is an urgent need to develop affordable, earth-abundant alkaline HER electrocatalysts with high performance.

Transition metal-based catalysts, such as sulfides, selenides, phosphides, and carbides, have garnered significant research interest as viable substitutes for noble metal-based electrocatalysts to enhance the kinetics of the HER.[1,8] Although these

[a]*Graduate Institute of Applied Science and Technology, National Taiwan University of Science and Technology, Taipei 10607, Taiwan. E-mail: cccheng@mail.ntust.edu.tw*
[b]*Advanced Membrane Materials Research Center, National Taiwan University of Science and Technology, Taipei 10607, Taiwan*
[c]*Department of Materials Science and Engineering, National Taiwan University of Science and Technology, Taipei 10607, Taiwan*
[d]*Department of Anatomy and Cell Biology, School of Medicine, College of Medicine, Taipei Medical University, Taipei, 11031, Taiwan. E-mail: ammielee@tmu.edu.tw*

materials typically display great activity and stability in acidic environments, their performance in alkaline media remains limited due to lower catalytic activity or poor stability.[9–12] For example, tungsten disulfide (WS_2), one of the two-dimensional transition metal dichalcogenides (TMDs), holds great potential for applications due to its favorable hydrogen adsorption energy at edge sites, inherent stability, and high activity for the HER in acidic media.[13,14] However, the performance of WS_2 in alkaline media is hindered by poor conductivity, strong hydroxide adsorption, and sluggish water dissociation kinetics; these issues stem from structural and electronic properties.[15,16] Despite extensive efforts, strong hydrogen evolution activity remains largely confined to acidic environments, while the reaction kinetics in the more practically viable alkaline media are relatively sluggish.[17,18] Similarly, due to the intrinsic properties of molybdenum disulfide (MoS_2), including inefficient water adsorption and dissociation caused by an unfavorable alignment of orbitals, MoS_2, a member of the TMDs, also exhibits limited activity in alkaline hydrogen evolution catalysis.[19,20] Thus, due to these limitations, development of hybrid materials or improvements to existing catalysts are necessary to enhance the performance of the HER across a broader pH range.

Researchers have employed various strategies with the aim of accelerating the overall kinetics of the HER under alkaline conditions, such as creating a nanoscale morphology and size modulation of WS_2, heteroatom doping, defect engineering, and construction of heterostructures. Multiple functional components have been integrated into hybrid heterostructure systems in attempts to optimize various steps of the HER process.[16] For example, combining WS_2 with water dissociation promoters or conductive polymers enhanced electron transfer, improved mass transport, and increased the density of exposed active sites. Feng *et al.* prepared a trinickel disulfide (Ni_3S_2)/MoS_2 heterostructure to demonstrate that modulation of the interfacial and electronic structure of MoS_2 could enhance its performance in the alkaline HER. Specifically, the integration of Ni_3S_2 promotes H_2O adsorption and dissociation and thereby improves the overall alkaline HER kinetics of the Ni_3S_2/MoS_2 composite.[16] Moreover, Hussain *et al.* developed a tungsten carbide (W_2C)/WS_2 hybrid that exhibited remarkable electrocatalytic performance in both alkaline and acidic conditions. The heterostructure exhibited enhanced performance, as evidenced by overpotentials (η_{10}) of 133 mV and 105 mV at 10 mA cm^{-2}, along with Tafel slopes of 70 mV dec^{-1} and 84 mV dec^{-1}, respectively.[21] Similarly, Hussain *et al.* also fabricated a molybdenum carbide (Mo_2C)@WS_2 hybrid *via* a simple chemical method. The resulting heterostructure electrocatalyst exhibited low Tafel slopes of 59 and 95 mV dec^{-1} and low overpotentials of 93 mV and 98 mV at 10 mA cm^{-2} in acidic and alkaline solutions, respectively, during the HER.[22] The formation of heterostructures between two active components induces a non-equilibrium state in the catalyst. This generates charged interfacial regions and strong built-in electric fields, which significantly alter the electronic density of interfacial atoms. The built-in electric field at the interface can enhance catalytic activity by accelerating charge transfer, improving conductivity, and optimizing the electronic structure.[23] Significant progress has been made through techniques such as heteroatom doping, defect engineering, and heterostructure formation.[24] However, the challenging issues related to interfacial compatibility and stability between components—which arise from differences in material properties—continue to limit the electrocatalytic performance of electrodes for the HER.[25,26] Even with optimized structural and compositional tuning, the improvements are still quite limited.[27]

To overcome the challenges of interfacial compatibility and stability, many research groups have focused on exploring various approaches to enhance the electrocatalytic activity and stability of WS_2 under different environmental conditions. For example, the creation of a heterojunction interface between WS_2 and the zirconium-based metal–organic framework UiO-66 induces synergistic interactions that facilitate efficient charge transfer and thereby significantly enhanced HER/OER activity under alkaline conditions.[28] Similarly, Zhang *et al.* developed a sea-anemone-like core–shell heterojunction composed of oxygen-vacancy-rich CoP@CoOOH on a carbon paper substrate, which exhibited remarkable HER catalytic performance in both alkaline and neutral media. This enhancement was ascribed to a synergistic interaction between the core and shell constituents.[29] Recently, our team employed an integrated strategy combining sodium-carboxymethyl chitosan (Na-CMC)-assisted exfoliation, electropolymerization (EP), and electrochemical activation (EA) to couple P-type PANI with N-type WS_2 on nickel foam, thereby creating an intrinsic P–N heterojunction electrode assigned as Na-CMC/WS_2/PANI/NF. This design improved interfacial compatibility between PANI and WS_2, facilitated efficient charge transport, increased the density of accessible catalytic active sites, and accelerated the reaction kinetics. Consequently, the electrodes demonstrated excellent HER electrocatalytic performance and long-term structural stability in acidic media.[26] These findings also demonstrate that the presence of a P–N heterojunction within the material matrix not only represents an effective strategy to enhance interfacial compatibility and structural stability but also facilitates stable charge transport across the interface to thereby achieve the desired electrocatalytic performance. Therefore, we confidently propose that incorporating a P–N heterojunction into the WS_2 matrix can markedly improve its long-term structural stability and overall electrocatalytic performance for the HER in alkaline environments. This strategy not only mitigates the intrinsic instability of WS_2 under alkaline conditions but also unlocks its capabilities as a noble-metal-free electrocatalyst for diverse energy conversion applications.

In this work, we fabricated a Na-CMC/WS_2/PANI/NF electrode featuring P–N heterojunction interfaces through a process involving Na-CMC-assisted exfoliation, EP, and EA. This electrode not only effectively overcomes the inherent structural instability of WS_2 under alkaline conditions, but also exhibits excellent HER catalytic activity in alkaline media. Electrocatalytic HER evaluation demonstrated that the fabricated electrode exhibits outstanding electrocatalytic activity in a 1.0 M potassium hydroxide (KOH) solution after electroactivation processing treatment. This performance was defined by an η_{10} of 24.5 mV with a Tafel slope of 48.2 mV dec^{-1} and a resistance of approximately 0.5 Ω, demonstrating results on par with those

of commercial Pt/C electrocatalysts. Importantly, unlike Pt/C, which suffers notable performance loss after 1000 cycles of cyclic voltammetry (CV) and 24 h of continuous operation at 100 mA cm^{-2}, the activated electrode (Na-CMC/WS_2/PANI/NF) maintains high catalytic activity and structural integrity. Therefore, this newly developed strategy for constructing P–N heterojunctions offers an effective approach to overcome the intrinsic limitations of WS_2 for the HER under alkaline conditions and may help to enable the realization of cost-effective and high-efficiency WS_2-based HER electrocatalysts with promising potential to replace Pt/C catalysts in various energy-related applications.

2. Experimental section

2.1 Materials

All materials used in this study were of the highest available purity. Specifically, pristine WS_2 (325 mesh, 99.9% metals basis), aniline (99.5%, extra pure), chitosan powder (degree of deacetylation > 85%, molecular weight ≈ 200 000 g mol^{-1}), and KOH (85%) were purchased from Thermo Scientific Chemicals. Sulfuric acid (H_2SO_4, 97%) and hydrochloric acid (HCl, 37%) were obtained from Honeywell Research Chemicals and used as received without further purification. NF, supplied by MTI Corporation, had a high purity (>99.96%), a density of 346 g m^{-2}, a thickness of 1.6 mm, and a porosity greater than 95%. The synthesis of Na-CMC and Na-CMC-functionalized exfoliated WS_2 nanosheets followed the procedures outlined in our previously published work.[26,30] Additional materials used include 20% Pt/C as a reference catalyst, Nafion solution as a binder, Pt wire and graphite rod as counter electrodes, and a silver/silver chloride (Ag/AgCl) electrode as the reference electrode.

2.2 Preparing a WS_2 dispersion *via* exfoliation

Few-layered tungsten disulfide nanosheets were prepared using a liquid-phase exfoliation technique, as described in our prior work.[26,30] Briefly, 1.0 mg mL^{-1} sodium carboxymethyl chitosan (Na-CMC) solution was prepared by dissolving the polymer salt in deionized water. Bulk WS_2 powder was then dispersed into the Na-CMC solution at a mass ratio of 1 : 3 (Na-CMC : WS_2) and subjected to ultrasonication for 30 minutes at 50% amplitude utilizing a probe sonicator (Q700, Osonica, Newtown, CT, USA), while maintaining the temperature below 5 °C using an ice bath. The resulting dark green suspension was filtered and centrifuged at 4000 rpm for 10 min to remove unexfoliated materials. The upper ~85% of the supernatant was carefully harvested for subsequent analysis and electrode fabrication.

2.3 Electropolymerization of Na-CMC/WS_2/PANI on nickel foam (NF)

Composite films of WS_2 nanosheets and polyaniline (PANI) were fabricated on NF substrates by EP with an SP-200 Potentiostat/Galvanostat (Bio-Logic, Knoxville, TN, France), following a previously optimized protocol.[26] Electrochemical characterizations were carried out utilizing a three-electrode system, with a platinum wire as the auxiliary electrode and an Ag/AgCl electrode as the reference electrode, while NF (1.0 cm^2) with active electrocatalysts served as the working electrode. The electrodes designated as Na-CMC/WS_2/PANI/NF were fabricated through EP utilizing an electrolyte solution consisting of exfoliated WS_2 dispersion and aqueous anilinium chloride mixed at a 1 : 2 volume ratio. This polymerization process was carried out at a constant current (0.10 mA) for a duration of 40 minutes. After deposition, the resulting electrodes were cleaned carefully with DI water to eliminate any loosely bound species and residual aniline salts and then dried under ambient conditions. For comparison, PANI was electrodeposited on NF under identical conditions from a saturated anilinium chloride solution without WS_2, resulting in PANI/NF control electrodes. The successful electropolymerization and nanosheets incorporation were evidenced by a greenish coloration of the NF substrate and a concurrent decrease in potentiometric response.

2.4 Electrochemical activation of modified electrodes

The modified electrodes were electrochemically activated (EA) in 0.5 M H_2SO_4 using chronopotentiometry at 500 mA cm^{-2} for 4 h to enhance their electrocatalytic performance. This activation step is essential for raising the availability of active sites and improving electrode stability. After activation, the electrodes were washed thoroughly with deionized water to remove any residual electrolyte.

2.5 Deposition of Pt/C on nickel foam

For comparison, a Pt/C catalyst layer was deposited onto the NF. A catalyst ink was prepared by dispersing 5.0 mg of commercial 20 wt% Pt/C in a 900 μL water-isopropanol mixture (4 : 5 v/v) and 100 μL of 5 wt% Nafion solution. This mixture was sonicated for 30 min to ensure uniform dispersion. Subsequently, 250 μL of the ink was drop-cast onto a 1 × 1 cm^2 NF substrate and dried naturally to obtain the Pt/C/NF electrode.

2.6 Characterizations

Advanced characterization techniques were used to examine the structure, morphology, and composition of the Na-CMC/WS_2 composite nanomaterials. X-ray diffraction (XRD) was used to determine the crystalline phase and interlayer spacing, and transmission electron microscopy (TEM) and scanning electron microscopy (SEM) were utilized to observe the surface morphology and nanoscale architecture. Elemental composition mapping was conducted using SEM coupled with energy dispersive X-ray (EDX) spectroscopy. Raman spectroscopy was performed to confirm the functionalization of WS_2 with Na-CMC and assess the chemical bonding and structural integrity of the composite. The Mott–Schottky curves, energy band analysis, and electron microscopy images confirmed the formation of a P–N heterojunction between exfoliated WS_2 nanosheets and PANI in the electrode. In addition, a series of electrochemical analyses confirmed that the EA-treated Na-CMC/WS_2/PANI/NF exhibited excellent hydrogen evolution catalytic performance in acidic environments. The specific operating methods of these techniques and their result discussions were detailed in our previous study.[26]

2.6.1 Raman spectra. Were obtained using a Raman spectrometer (Jasco NRS-5100, Tokyo, Japan) with a 532 nm helium-neon laser as the excitation source. Measurements were conducted within the spectral range of 200–500 cm^{-1} at a resolution of 1.09 cm^{-1} using a 20× objective lens at 25 °C. Prior to Raman analysis, the NF samples, with the deposited active nanomaterials, were sectioned, dehydrated under vacuum, and directly subjected to spectroscopic evaluation.

2.6.2 SEM. The active material deposited on the NF substrate was further analyzed by cutting the NF into smaller pieces, drying the pieces in a vacuum oven, and then directly subjecting the samples to morphological analysis with a high-resolution field emission SEM (JSM-6500F, JEOL, Tokyo, Japan). Elemental composition and distribution were assessed using EDX spectroscopy (Thermo Scientific Ultra Dry SDD EDS, dual detector with NSS software) at an accelerating voltage of 15.0 kV using an aluminum sample holder and also assessed using an elemental analyzer (Flash 2000, Thermo Fischer Scientific, Bremen, Germany).

2.6.3 Evaluation of electrochemical performance. Electrochemical analysis was evaluated at ambient temperature utilizing a three-electrode setup integrated with an SP-200 Potentiostat, operating within a 1.0 M KOH electrolyte solution (pH 13.6). To evaluate HER activity, Na-CMC/WS_2 composites were incorporated into working electrodes by depositing the nanosheets and PANI onto NF substrates *via* EP, followed by EA. The working electrode was the modified NF electrode (1 × 1 cm^2), while the counter and reference electrodes were a graphite rod and an Ag/AgCl electrode.

2.6.4 Electrochemical measurements. Including linear sweep voltammetry (LSV), electrochemical impedance spectroscopy (EIS), and Tafel analysis, were conducted in 1.0 M KOH at room temperature to evaluate the HER activity of the prepared electrodes. The working electrodes (1 × 1 cm^2) were first activated by CV, cycling the potential between −1.4 V and 0.0 V *versus* Ag/AgCl at a scan rate of 100 mV s^{-1} for 30 cycles. This pretreatment cleaned the electrode surface, stabilized the electrochemical response, and enhanced catalytic performance. LSV was then conducted at a scan rate of 10 mV s^{-1}. EIS measurements were conducted at an overpotential of −0.91 V *vs.* Ag/AgCl across the frequency range from 200 kHz to 0.1 Hz at an amplitude of 10 mV AC. The resulting Nyquist plots were fitted using Randles equivalent circuit model. Tafel slopes were derived from the LSV curves to assess HER kinetics. The Nernst equation was employed to convert all observed potentials to the reversible hydrogen electrode (RHE) scale.

$$E_{RHE} = E_{Ag/AgCl} + 0.059\ pH + E^{\circ}_{Ag/AgCl}.$$

In addition, *iR* compensation to correct for voltage drops (*iR* drop) was applied to account for ohmic losses from the electrolyte and substrate.

2.7 Evaluation of the electrochemical stability of the fabricated electrodes

Stability testing of the developed electrodes was conducted using chronopotentiometry in 1.0 M KOH at a constant current density of 100 mA cm^{-2} for 24 h. The potential variation over time (*V*–*t* curves) was recorded following EA. Additionally, the long-term durability of the electrocatalyst toward the HER in alkaline conditions was assessed over 1000 consecutive CV cycles. Post-stability analysis of the electrodes was performed using SEM, EDX elemental mapping, and Raman spectroscopy to examine the morphological integrity, elemental distribution, and structural stability of the electrodes after prolonged electrochemical operation.

2.8 Electrochemical double-layer capacitance (C_{dl}) estimation for the fabricated electrodes

C_{dl} was measured by CV in the non-faradaic region (0.80–1.0 V *vs.* RHE) using 1.0 M KOH as the electrolyte. CV scans were performed at various scan rates (20–160 mV s^{-1}), and the capacitive current at 0.1 V was plotted against the scan rate. The slope of the linear fit was used to determine the C_{dl} value.

2.9 Catalytic activity was evaluated and compared using the following parameters

Overpotential (η) refers to the extra potential necessary to surmount the inherent kinetic barriers of electrochemical water splitting during both HER and OER. Under standard conditions, the equilibrium potentials for HER and OER are 0 V and 1.23 V *vs.* RHE respectively. The overpotential values for all tests were determined using the following equation, where 'E_{obs}' denotes the *iR*-compensated potential relative to RHE:

$$\eta(\mathrm{HER}) = (0 - E_{obs})\ \mathrm{V}\ \textit{vs.}\ \mathrm{RHE}.$$

The overpotential required to reach a current density of −10 mA cm^{-2}, denoted as η_{10}, was used as a benchmark to evaluate the electrocatalytic HER performance.

The Tafel slope provides crucial evidence about the rate-determining step and reaction mechanisms based on measuring the voltage change required to increase the electrochemical current by a factor of ten.[31]

The Tafel slopes were determined by fitting η as a function of the logarithm of the current density ($\log j$) using the Tafel equation, assuming uniform concentrations in the bulk solution and at the electrode–electrolyte interface:

$$\eta = b\ \log\left(\frac{J}{J_o}\right)$$

where b is the Tafel slope, J is the current density, and J_o is the exchange current density.

2.10 Statistical analysis

All electrochemical analyses and experiments were performed at least three times independently to confirm the reproducibility of the results.

3. Results and discussion

We recently developed a highly efficient HER electrocatalyst system featuring a P–N heterojunction interface. In this system,

water-soluble Na-CMC is employed to assist in the preparation of exfoliated N-type WS_2 nanosheets, which exhibit stable solid-state storage and reversible dispersion in aqueous media.[26] Integration with P-type PANI yielded a WS_2/PANI composite, forming a P–N heterojunction at the interface and considerably improving electrocatalytic activity in acidic media. Moreover, the composite displayed excellent structural integrity and stability, positioning it as a low-cost alternative to precious metal catalysts such as Pt/C for future hydrogen evolution applications. We therefore propose that Na-CMC-modified exfoliated WS_2 nanosheets, combined with a P–N heterojunction strategy, markedly enhance both the structural integrity and HER catalytic activity of exfoliated WS_2 under alkaline conditions (Scheme 1). This approach may help to effectively overcome the critical drawbacks related to structural instability that are commonly observed in WS_2 [17,18,32] and commercial Pt/C catalysts[33,34] during HER processes in alkaline environments. Prior to testing HER activity, the overall dispersion stability of exfoliated WS_2 nanosheets in alkaline solution was examined by varying the mixing ratios of Na-CMC and WS_2. The transmittance of the obtained 1/1, 1/3, and 1/5 Na-CMC/WS_2 dispersions at 500 nm was monitored over time using UV-vis spectroscopy at pH 13.5 and 25 °C. As shown in Fig. S1, the 1/3 and 1/5 dispersions exhibited only an 8% increase in transmittance after 63 days of monitoring, whereas the 1/1 dispersion increased by 48%, indicating that excess Na-CMC promotes WS_2 nanosheets self-aggregation.[25,26] Therefore, the 1/3 Na-CMC/WS_2 dispersion was selected as the reference solution for subsequent electrode preparation and evaluation of its electrocatalytic performance in the HER under alkaline conditions.

Upon integration with PANI, a stable P–N heterojunction forms between the N-type WS_2 nanosheets and the P-type polymer. This interfacial architecture is expected to improve electron mobility, facilitate transfer of charge between PANI and WS_2, and improve WS_2 structural stability in alkaline environments, ultimately boosting the overall HER performance. Therefore, we fabricated Na-CMC/WS_2/PANI/NF electrodes for the HER and investigated their electrochemical performance. Specifically, the designed composite electrode was constructed on a NF (1.0 cm^2 area) substrate *via* EP for 40 minutes.[26] Subsequently, the Tafel slopes and resistance of the resulting electrodes were evaluated using LSV and EIS in 1.0 M KOH. The HER performance of these electrodes was evaluated by LSV and EIS in 1.0 M KOH. As depicted in Fig. 1a–c, the developed electrode displayed reduced overpotential (η_{10}, 141.6 mV) and a Tafel slope (81.5 mV dec^{-1}) with a resistance of 17.6 Ω compared to blank nickel foam and PANI@NF electrodes. These findings confirm that combining N-type WS_2 nanosheets with P-type PANI effectively enhances the performance in the HER. Nevertheless, the HER performance of these electrodes in alkaline conditions is still significantly lower than that of the benchmark electrocatalyst (Pt/C), which exhibits an η_{10} of 21.8 mV with a Tafel slope of 45.3 mV dec^{-1} and a resistance of 0.8 Ω. Similar to the results obtained under acidic conditions, the EP-treated electrode showed an analogous trend in the alkaline environment.[26] This can be attributed to the interfacial

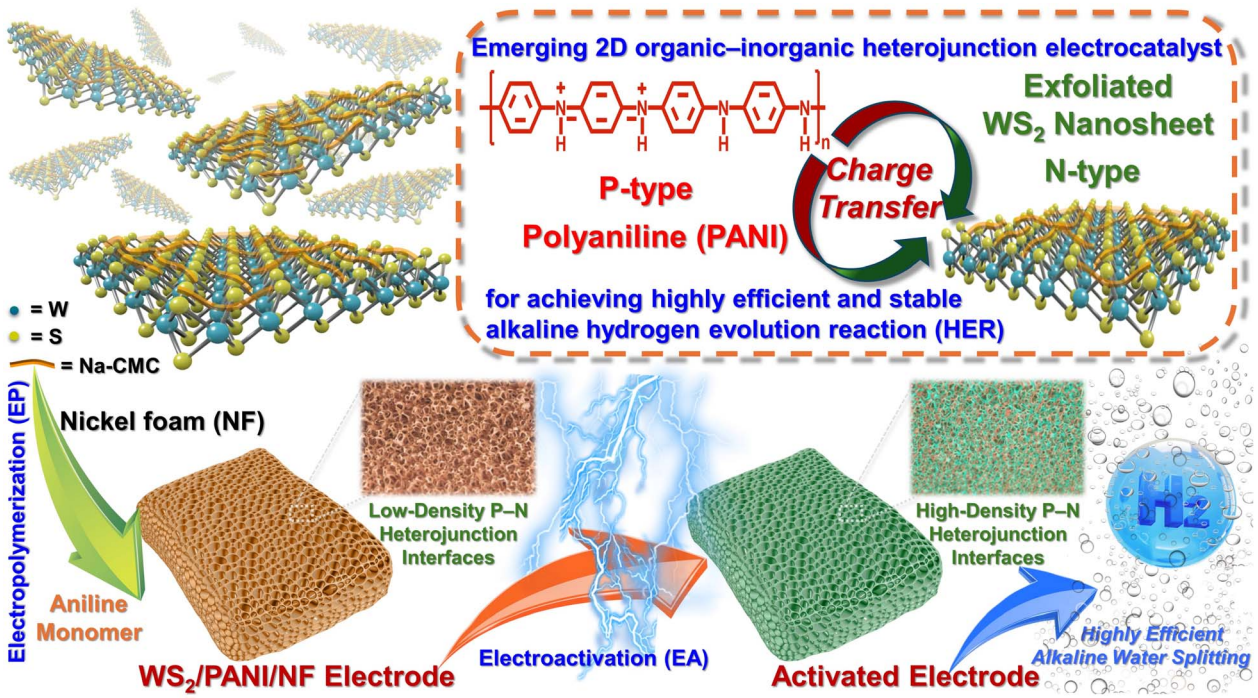

Scheme 1 Schematic of how exfoliated WS_2 nanosheets are used to construct a Na-CMC/WS_2/PANI/NF electrode with P–N heterojunction interfaces through electropolymerization and electroactivation processes, and thereby achieve excellent HER electrocatalytic performance in alkaline environments. The P–N heterojunction interface, depicted within the dashed box in the upper right corner, is established between the P-type PANI and N-type exfoliated WS_2 nanosheets. This interface plays a crucial role in promoting charge transfer from PANI to the WS_2 structure.

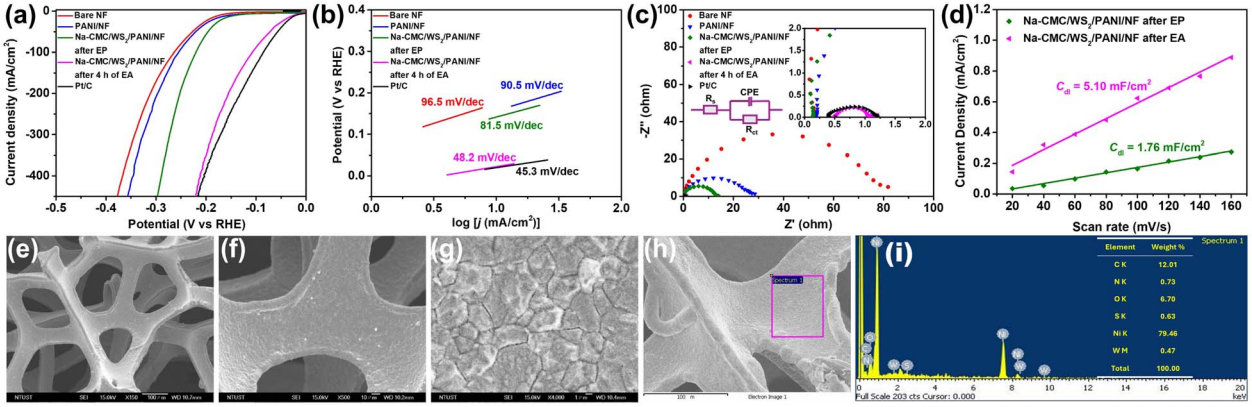

Fig. 1 HER performance of pristine nickel foam, PANI/NF, EP-treated Na-CMC/WS_2/PANI/NF, EA-treated Na-CMC/WS_2/PANI/NF, and commercial Pt/C in 1.0 M KOH solution: (a) LSV curves, (b) Tafel plots, and (c) EIS Nyquist plots. (c) The equivalent circuit (EC) model employed for fitting the experimental data is depicted in the left inset. Subsequently, data analysis is performed through fitting using this EC model. The EIS graph with a range of 0–2 ohm is shown in the right inset. (d) C_{dl} values for EP-treated and EA-treated fabricated electrodes in 1.0 M KOH solution. SEM images of the EA-treated developed electrode at magnifications of (e) ×150, (f) ×500, and (g) ×4000. (h) SEM image of the EA-treated fabricated electrode, along with (i) the corresponding EDX spectrum; the elemental weight percentage composition is displayed in the table.

incompatibility between the PANI and the exfoliated WS_2, which adversely affects the overall efficiency of HER catalysis.

To enhance the interfacial compatibility between the components, the fabricated electrode was treated *via* electrochemical activation at 500 mA cm^{-2}.[26] As depicted in Fig. S2a, the negative potential steadily reduced throughout the 12-h monitoring time and stabilized at approximately −0.4 V after around 2 h, suggesting that the high current density effectively promoted interfacial interactions between the components and led to the construction of high-density P–N heterojunctions. This interface is expected to enhance charge transfer and thereby improve the overall electrocatalytic performance. Furthermore, the electrocatalytic performance of the developed electrodes after varying periods of EA treatment was further evaluated using LSV and EIS. As depicted in Fig. S2b–d, electrodes subjected to varying periods of EA treatment exhibited similar electrochemical activity. For example, following a 4-h EA treatment, the electrode exhibited an η_{10} of 24.5 mV with a Tafel slope of 48.2 mV dec^{-1}, and a resistance of 0.5 Ω. Moreover, compared to the results achieved following EP treatment, the EA technique considerably boosted the catalytic activity of the exfoliated WS_2 nanosheets. Based on these findings and considering the optimized processing conditions, the fabricated electrode treated by EA for 4 h was selected for further investigation of its HER performance.

Further comparison with the Pt/C catalyst revealed that the EA-treated electrode (treated for 4 h) displayed comparable overpotential, Tafel slope, and resistance (Fig. 1a–c). This finding demonstrates that EA treatment boosts both HER activity and WS_2 stability in alkaline media through the generation of robust P–N heterojunctions. To further elucidate how EA treatment influences the electrocatalytic properties of the fabricated electrode, we investigated the changes in its electrochemically active surface area and surface morphology before and after EA treatment of the designed electrode. The Na-CMC/WS_2/PANI/NF electrodes showed C_{dl} values of 1.76 mF cm^{-2} after EP treatment and 5.10 mF cm^{-2} after EA treatment, as indicated in Fig. 1d and S3. The C_{dl} of the EA-treated electrode is approximately threefold higher than that of the EP-treated electrode. This enhancement confirms that EA treatment effectively increases the number of active catalytic sites and surface area, thereby significantly improving HER electrocatalytic performance.[35] In terms of surface morphology, SEM images revealed that the EA-treated electrode exhibited a uniform and textured surface morphology (Fig. 1e–g), in contrast to the rough and cracked surface of the electrode after EP treatment (Fig. S4). This indicates that the EA strategy facilitates improved interaction between PANI and WS_2 nanosheets, leading to the creation of stable P–N heterojunctions at their interface and thereby enhancing interfacial compatibility.

Furthermore, EDX spectroscopic examination, as illustrated in Fig. 1h, verified the presence of all anticipated elemental components on the surface of the activated Na-CMC/WS_2/PANI/NF electrode. The final electrode surface was found to contain 1.1 wt% of WS_2, as summarized in the table adjacent to Fig. 1i. Overall, these findings indicate that the EA treatment and the presence of P–N heterojunctions offer a strategy to bolster the structural integrity of WS_2 in alkaline conditions, substantially elevate its electrocatalytic activity, and consequently deliver exceptional alkaline HER performance.

Next, we surveyed recent WS_2-based electrocatalytic systems and summarized their reported HER performance. Table S1 clearly indicates that the EA-treated fabricated electrode exhibits a notably reduced overpotential and Tafel slope for HER electrocatalysis compared to various WS_2-based systems,[28,36–41] even with differences in substrate materials. This confirms that the presence of the P–N heterojunction interfaces in the electrode matrix not only greatly enhances the electrocatalytic activity of WS_2 but also effectively mitigates its intrinsic structural instability in alkaline environments[17,18,32] and may ultimately enable its potential extension to practical alkaline water electrolysis applications. Therefore, the strategy of

constructing the heterojunction interfaces presents a viable approach for developing highly effective and durable HER electrocatalysts in acidic as well as alkaline environments.[26]

Subsequent to confirming the electrocatalytic efficacy of the electrochemically activated electrode under alkaline conditions, we further evaluated its long-term stability by performing chronopotentiometry in 1 M KOH. The electroactivated electrode was operated at a fixed current density of 100 mA cm^{-2} for 24 h to evaluate its electrocatalytic durability. As depicted in Fig. 2a–d, the LSV curves, Tafel slopes, and resistance values remained virtually unchanged after continuous operation at a current density of 100 mA cm^{-2} for 24 h, indicating excellent durability. This result demonstrates the excellent structural stability of the EA-treated electrode enables it to maintain stable HER catalytic performance over time. Similar results were observed in a long-term CV stability evaluation. As shown in Fig. 2e–h, the activated electrode exhibited negligible variations in electrocatalytic activity after 1000 consecutive CV cycles. This clearly indicates that the P–N heterojunction interface within the composite electrode matrix is critical for maintaining the structural stability of WS_2 nanosheets, which in turn ensures consistently efficient HER performance in alkaline environments.[42] In contrast, the electrocatalytic activity of Pt/C for the HER is substantially diminished in alkaline environments. After either a continuous 24-h test at 100 mA cm^{-2} (Fig. 3a–d) or following 1000 CV cycles (Fig. 3e–h), Pt/C exhibited significantly deteriorated performance in 1 M KOH compared to its initial state. Specifically, the overpotential of Pt/C at −10 mA cm^{-2} increased to 30.2 mV after the 24-h test (Fig. 3b) and rose further to 35.8 mV after 1000 CV cycles (Fig. 3f). In addition, the Tafel slope of Pt/C increased to 71.8 mV dec^{-1} after the 24-h test (Fig. 3c) and reached 93.0 mV dec^{-1} following the CV cycling (Fig. 3g). The decline in the electrocatalytic efficiency of Pt/C under alkaline conditions can be attributed to several key factors. Firstly, in alkaline media, platinum tends to undergo oxidation, which leads to the formation of surface species such as platinum oxide (PtO) or platinum hydroxide [$Pt(OH)_2$]. This process reduces the number of active catalytic sites and alters the electronic structure of platinum and ultimately decreases its activity in reactions such as hydrogen evolution and oxygen reduction.[43] Secondly, under alkaline conditions and at high operating potentials, the carbon support gradually undergoes degradation. This degradation leads to the detachment and loss of the Pt nanoparticles dispersed on the carbon matrix and thereby reduces the overall active surface area and compromises catalytic performance.[44] Finally, in alkaline environments, due to their high concentration, hydroxide ions (OH^-) tend to adsorb onto the surface of Pt and block the active sites.[3,45] This not only reduces catalytic activity but also promotes the formation of large Pt clusters and aggregates.[46,47] Based on the discussion above, our findings readily confirm that the electroactivated electrode demonstrates excellent electrocatalytic stability under alkaline conditions and holds significant promise as a viable alternative to noble metal Pt/C catalysts, achieving the desired performance for hydrogen production *via* water electrolysis. The above results inspired our curiosity to further investigate the structural attributes, surface morphology, and elemental distribution of the electrodes after the long-term stability tests.

Raman spectroscopy analysis (Fig. S5) revealed that the exfoliated WS_2 nanosheets in the EA-treated electrode retained their structural integrity after testing at a current density of 100 mA cm^{-2} and 1000 cycles of CV, compared to the pristine EA-treated electrode, indicating good structural stability. This result suggests that the exfoliated WS_2 nanosheets exhibit excellent enduring catalytic stability and resilience to alkaline environments, which can be attributed to the presence and protective effect of the P–N heterojunctions within the

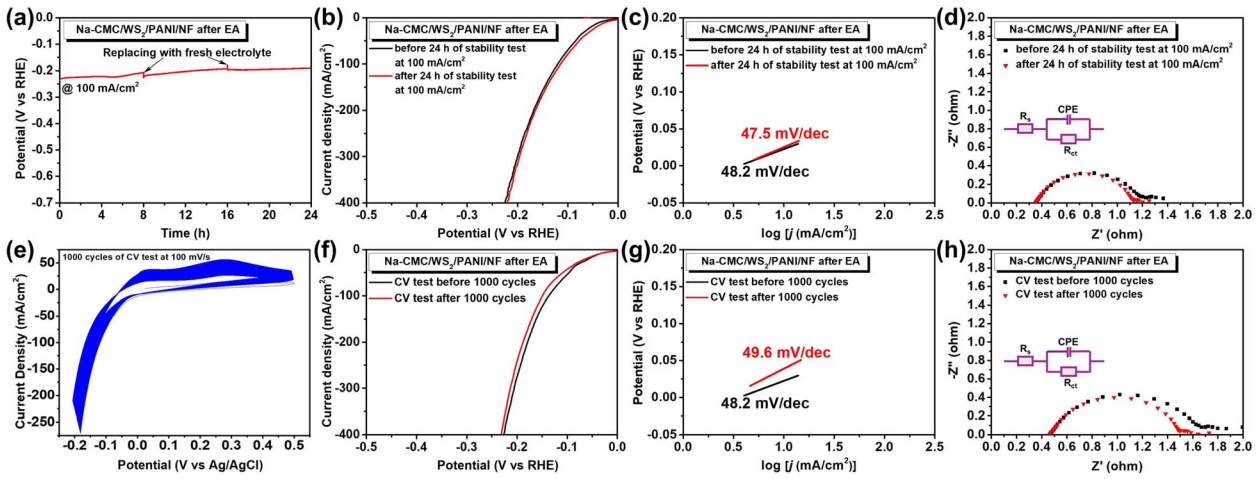

Fig. 2 (a) Chronopotentiometric curve for the EA-treated Na-CMC/WS_2/PANI/NF electrode operated continuously at a fixed current density of 100 mA cm^{-2} for 24 h in 1.0 M KOH solution. HER activity of the EA-treated fabricated electrode in 1.0 M KOH solution before and after 24 h testing at 100 mA cm^{-2}: (b) LSV curve, (c) Tafel plot, and (d) EIS Nyquist plot. (e) CV curves for the EA-treated fabricated electrode after 1000 cycles at a scan rate of 100 mV s^{-1} in 1.0 M KOH solution. (f) LSV curves, (g) Tafel plots, and (h) EIS Nyquist plots for the EA-treated fabricated electrode before and after 1000 CV cycles in 1.0 M KOH solution. (d and h) The insets on the left show the EC models used to fit the experimental data.

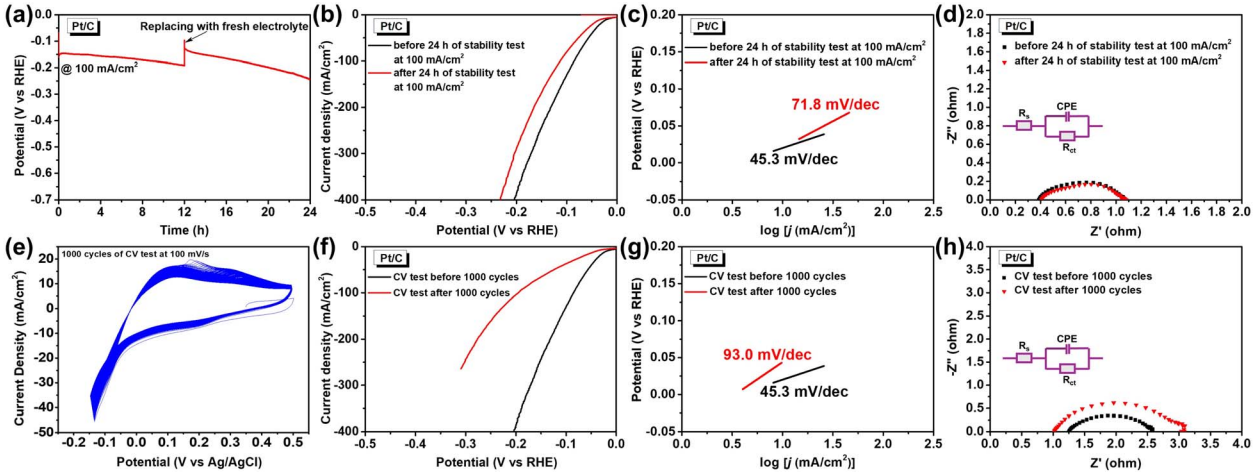

Fig. 3 (a) Chronopotentiometric curve for the Pt/C electrocatalyst operated continuously at a constant current density of 100 mA cm^{-2} for 24 h in 1.0 M KOH solution. HER performance of the Pt/C electrocatalyst in 1.0 M KOH before and after 24 h of operation at 100 mA cm^{-2}: (b) LSV curve, (c) Tafel plot, and (d) EIS Nyquist plot. (e) CV curves for the Pt/C electrocatalyst after 1000 cycles at a scan rate of 100 mV s^{-1} in 1.0 M KOH. (f) LSV curves, (g) Tafel plots, and (h) EIS Nyquist plots comparing the Pt/C electrocatalyst before and after 1000 CV cycles in 1.0 M KOH. (d and h) The inset on the left shows the EC model used to fit the experimental data.

electrode. The same outcomes were also noted in SEM measurements. The surface and microstructural morphologies of the EA-treated composite electrode remained largely unchanged after 24 h of continuous process at 100 mA cm^{-2} (as depicted in Fig. 4a–e) and after 1000 CV cycles (Fig. 4m–q), when compared to their pristine states (Fig. 1e–i). Furthermore, all characteristic elemental components remained present in the structure (Fig. 4e and q), further indicating the excellent

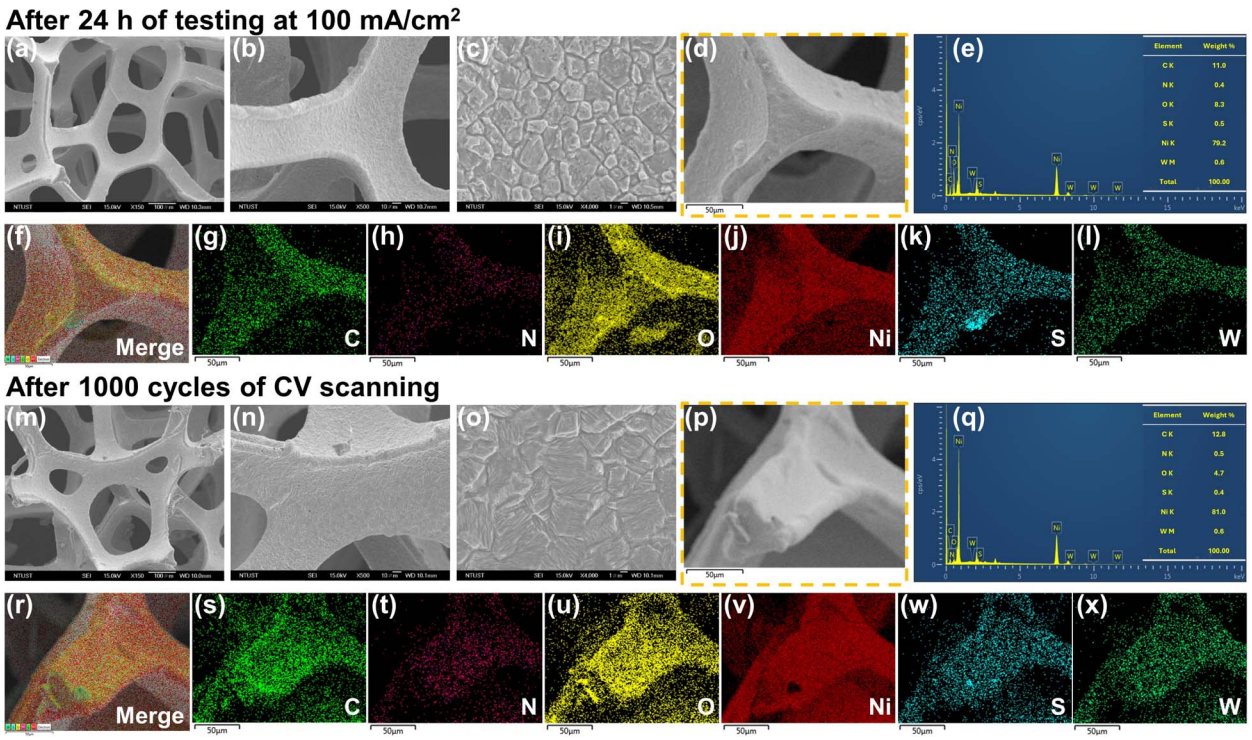

Fig. 4 SEM images of the EA-treated Na-CMC/WS_2/PANI/NF electrode after 24 h operation at 100 mA cm^{-2} in 1.0 M KOH solution, at magnifications of (a) ×150, (b) ×500, and (c) ×4000. (d) SEM image of the EA-treated electrode after 24 h of operation at 100 mA cm^{-2}, along with (e) the corresponding EDX spectrum; the elemental % wt composition is displayed in the table in the upper right corner. Elemental mapping images of (f) merged elements, (g) C, (h) N, (i) O, (j) Ni, (k) S, and (l) W for the EA-treated fabricated electrode after 24 h of testing at 100 mA cm^{-2}. SEM images of the EA-treated fabricated electrode after 1000 CV cycles in 1.0 M KOH solution, at magnifications of (m) ×150, (n) ×500, and (o) ×4000. (p) SEM image of the EA-fabricated electrode after 1000 CV cycles, along with (q) the corresponding EDX spectrum; the elemental wt% composition is displayed in the table in the upper right corner. Elemental mapping images of (r) merged elements, (s) C, (t) N, (u) O, (v) Ni, (w) S, and (x) W for the EA-treated fabricated electrode after 1000 CV cycles.

structural stability of the EA-treated electrode. It is worth noting that, compared to the pre-test results (right table in Fig. 1i), the WS_2 content (wt%) of the EA-treated electrode did not significantly change after both stability tests (top-right tables in Fig. 4e and q). This finding reveals that the WS_2 nanosheets remained stably anchored to the electrode surface, even after prolonged exposure to high current density or continuous CV cycling. Moreover, elemental mapping images, acquired *via* EDX integrated with SEM, further corroborated the presence and uniform distribution of all distinctive elements across the surface of the EA-treated electrodes following both stability tests (Fig. 4f–l, and r–x). This further supports our observation that the presence of P–N heterojunctions within the electrode matrix not only contributes to the structural integrity of the electrode but also facilitates charge flow from PANI to the WS_2 structure throughout the HER process. Consequently, WS_2 can stably and efficiently catalyze hydrogen evolution, ultimately achieving the desired performance for water electrolysis in an alkaline environment.

4. Conclusions

A Na-CMC/WS_2/PANI/NF electrode was successfully fabricated, featuring a P–N heterojunction interface that demonstrates remarkable structural stability and enhanced electrocatalytic activity for the HER in an alkaline environment. This electrode effectively addresses the inherent structural instability of WS_2 in alkaline environments, positioning it as a promising non-noble-metal electrocatalyst with significant potential to substitute commercial Pt/C catalysts across diverse energy-related applications. In this study, Na-CMC was used as an exfoliant for WS_2 crystals, producing exfoliated WS_2 nanosheets that exhibited stable dispersion in alkaline aqueous environments over an extended period. Na-CMC not only promotes exfoliation but also improves the structural resilience of WS_2 nanosheets in alkaline conditions. Subsequently, p-type PANI and n-type exfoliated WS_2 nanosheets were integrated onto a nickel foam substrate through EP and EA processing, forming a stable organic-inorganic P–N heterojunction interface. This electrode exhibited excellent electrocatalytic activity, with a small η_{10} of 24.5 mV, a Tafel slope of 48.2 mV dec^{-1}, and low resistance ($\sim$5 Ω), comparable to commercial Pt/C catalysts. After 1000 cycles of CV and 24 h of continuous operation at a current density of 100 mA cm^{-2}, the electrode maintained outstanding long-term electrocatalytic performance and structural integrity. In contrast, the Pt/C catalyst exhibited significant performance degradation under the same conditions. These results demonstrate that the P–N heterojunction effectively promotes stable HER catalysis by WS_2 nanosheets under alkaline conditions, enabling high-efficiency hydrogen production *via* water electrolysis. Overall, this newly developed strategy based on the construction of a P–N heterojunction offers a novel and efficient approach to overcoming the intrinsic limitations of WS_2 in alkaline environments and paves the way for a high-activity, low-cost, pH-universal electrocatalyst for hydrogen evolution *via* water electrolysis.

Conflicts of interest

The authors declare no competing financial interest.

Note added after first publication

This article replaces the version published on 16 December 2025, which contained an incorrect Fig. 1.

Data availability

The author confirms that all data generated or analysed during this study are included in this published article.

Supplementary information (SI): includes supplementary characterization and electrochemical data. See DOI: https://doi.org/10.1039/d5ra08680a.

Acknowledgements

National Science and Technology Council, Taiwan (contract no. NSTC 113-2221-E-011-007-MY3, 114-2221-E-011-030 and 114-2218-E-011-002) and National Taiwan University of Science and Technology – Taipei Medical University Joint Research Program (contract no. NTUST-TMU-112-04). This study was supported financially by the National Science and Technology Council, Taiwan (contract no. NSTC 113-2221-E-011-007-MY3, 114-2221-E-011-030 and 114-2218-E-011-002) and National Taiwan University of Science and Technology – Taipei Medical University Joint Research Program (contract no. NTUST-TMU-112-04).

References

1 Z. W. Seh, J. Kibsgaard, C. F. Dickens, I. Chorkendorff, J. K. Nørskov and T. F. Jaramillo, *Science*, 2017, **355**, eaad4998.
2 S. Sultan, J. N. Tiwari, A. N. Singh, S. Zhumagali, M. Ha, C. W. Myung, P. Thangavel and K. S. Kim, *Adv. Energy Mater.*, 2019, **9**, 1900624.
3 N. Mahmood, Y. Yao, J.-W. Zhang, L. Pan, X. Zhang and J.-J. Zou, *Adv. Sci.*, 2018, **5**, 1700464.
4 Y. Zheng, Y. Jiao, A. Vasileff and S.-Z. Qiao, *Angew. Chem., Int. Ed.*, 2018, **57**, 7568–7579.
5 J. Wei, M. Zhou, A. Long, Y. Xue, H. Liao, C. Wei and Z. J. Xu, *Nano-Micro Lett.*, 2018, **10**, 75.
6 A. Guha, M. Sahoo, K. Alam, D. K. Rao, P. Sen and T. N. Narayanan, Role of water structure in alkaline water electrolysis, *iScience*, 2022, **25**, 104835.
7 S. Zhou, W. Cao, L. Shang, Y. Zhao, X. Xiong, J. Sun, T. Zhang and J. Yuan, *Nat. Commun.*, 2025, **16**, 1849.
8 S. Anantharaj, S. R. Ede, K. Sakthikumar, K. Karthick, S. Mishra and S. Kundu, *ACS Catal.*, 2016, **6**, 8069–8097.
9 T.-W. Lee and C. Chen, Influence of Inorganic Anions on the Chemical Stability of Molybdenum Disulfide Nanosheets in the Aqueous Environment, *Environ. Sci. Technol.*, 2024, **58**, 2490–2501.

10 Z. Wang, A. von dem Bussche, Y. Qiu, T. M. Valentin, K. Gion, A. B. Kane and R. H. Hurt, *Environ. Sci. Technol.*, 2016, **50**, 7208–7217.
11 L. Xie, L. Wang, W. Zhao, S. Liu, W. Huang and Q. Zhao, *Nat. Commun.*, 2021, **12**, 5070.
12 T. F. Jaramillo, K. P. Jørgensen, J. Bonde, J. H. Nielsen, S. Horch and I. Chorkendorff, *Science*, 2007, **317**, 100–102.
13 L. Cheng, W. Huang, Q. Gong, C. Liu, Z. Liu, Y. Li and H. Dai, *Angew. Chem., Int. Ed.*, 2014, **53**, 7860–7863.
14 X. Zhao, X. Ma, J. Sun, D. Li and X. Yang, *ACS Nano*, 2016, **10**, 2159–2166.
15 J. D. Wiensch, J. John, J. M. Velazquez, D. A. Torelli, A. P. Pieterick, M. T. McDowell, K. Sun, X. Zhao, B. S. Brunschwig and N. S. Lewis, *ACS Energy Lett.*, 2017, **2**, 2234–2238.
16 J. Feng, Z. Zhao, R. Tang, Y. Zhao and T. Meng, *ACS Appl. Mater. Interfaces*, 2021, **13**, 53262–53270.
17 L. Xie, L. Wang, X. Liu, J. Chen, X. Wen, W. Zhao, S. Liu and Q. Zhao, *Nat. Commun.*, 2024, **15**, 5702.
18 L. Liao, Y. Zhao, H. Zhou, D. Li, Y. Qi, Y. Zhang, Y. Sun, Q. Zhou and F. Yu, *Small*, 2022, **18**, 2203171.
19 Y. Zang, S. Niu, Y. Wu, X. Zheng, J. Cai, J. Ye, Y. Xie, Y. Liu, J. Zhou, J. Zhu, X. Liu, G. Wang and Y. Qian, *Nat. Commun.*, 2019, **10**, 1217.
20 J. Hu, C. Zhang, L. Jiang, H. Lin, Y. An, D. Zhou, M. K. H. Leung and S. Yang, *Joule*, 2017, **1**, 383–393.
21 S. Hussain, I. Rabani, D. Vikraman, A. Feroze, M. Ali, Y.-S. Seo, H.-S. Kim, S.-H. Chun and J. Jung, *Nanomaterials*, 2020, **10**, 1597.
22 S. Hussain, D. Vikraman, M. Hussain, H.-S. Kim and J. Jung, *Catalysts*, 2021, **11**, 1060.
23 X. Zhao, M. Liu, Y. Wang, Y. Xiong, P. Yang, J. Qin, X. Xiong and Y. Lei, *ACS Nano*, 2022, **16**, 19959–19979.
24 J. Hu, A. Al-Salihy, J. Wang, X. Li, Y. Fu, Z. Li, X. Han, B. Song and P. Xu, *Adv. Sci.*, 2021, **8**, 2103314.
25 C.-Y. Tsai, H.-S. Li, K. K. Kuchayita, H.-C. Huang, W.-N. Su and C.-C. Cheng, *Adv. Sci.*, 2024, **11**, 2407061.
26 Y. A. Fesseha, K. K. Kuchayita, W.-N. Su, C.-W. Chiu and C.-C. Cheng, *Chem. Eng. J.*, 2025, **509**, 161501.
27 J. Wu, X. Gao and Z. Chen, *Chem. Eng. J.*, 2024, **492**, 152241.
28 M. Shah, U. Abdullah, E. Pervaiz and M. Ali, *Energy Adv.*, 2024, **3**, 459–470.
29 B. Zhang, J. Shan, W. Wang, P. Tsiakaras and Y. Li, *Small*, 2022, **18**, 2106012.
30 K. K. Kuchayita, H.-S. Li, M. Tokita and C.-C. Cheng, *FlatChem*, 2025, **51**, 100844.
31 C. Wan, Y. Ling, S. Wang, H. Pu, Y. Huang and X. Duan, *ACS Cent. Sci.*, 2024, **10**, 658–665.
32 M. Ďurovič, J. Hnát and K. Bouzek, *J. Power Sources*, 2021, **493**, 229708.
33 A. Zadick, L. Dubau, N. Sergent, G. Berthomé and M. Chatenet, *ACS Catal.*, 2015, **5**, 4819–4824.
34 M. F. Labata, G. Li, J. Ocon and P.-Y. A. Chuang, *J. Power Sources*, 2021, **487**, 229356.
35 S. I. Perez Bakovic, P. Acharya, M. Watkins, H. Thornton, S. Hou and L. F. Greenlee, *J. Catal.*, 2021, **394**, 104–112.
36 Q. Zhu, W. Chen, H. Cheng, Z. Lu and H. Pan, *ChemCatChem*, 2019, **11**, 2667–2675.
37 L. Sun, M. Gao, Z. Jing, Z. Cheng, D. Zheng, H. Xu, Q. Zhou and J. Lin, *Chem. Eng. J.*, 2022, **429**, 132187.
38 J. Wu, T. Chen, C. Zhu, J. Du, L. Huang, J. Yan, D. Cai, C. Guan and C. Pan, *ACS Sustainable Chem. Eng.*, 2020, **8**, 4474–4480.
39 H. Belhadj, W. Boughouiche, N. Boumazza, Y. Messaoudi, I. Belkhettab, M. R. Khelladi and A. Azizi, *Surf. Interfaces*, 2025, **65**, 106447.
40 F. Rasool, B. M. Pirzada, S. H. Talib, T. Alkhidir, D. H. Anjum, S. Mohamed and A. Qurashi, *ACS Appl. Mater. Interfaces*, 2024, **16**, 14229–14242.
41 H. Chen, M. Hu, P. Jing, B. Liu, R. Gao and J. Zhang, *J. Power Sources*, 2022, **521**, 230948.
42 K. K. Kuchayita and C.-C. Cheng, *J. Mater. Chem. A*, 2025, **13**, 34249–34259.
43 M. A. van Spronsen, J. W. M. Frenken and I. M. N. Groot, *Nat. Commun.*, 2017, **8**, 429.
44 Z. Zhao, L. Castanheira, L. Dubau, G. Berthomé, A. Crisci and F. Maillard, *J. Power Sources*, 2013, **230**, 236–243.
45 A. A. Feidenhans'l, Y. N. Regmi, C. Wei, D. Xia, J. Kibsgaard and L. A. King, *Chem. Rev.*, 2024, **124**, 5617–5667.
46 F. Maillard, S. Schreier, M. Hanzlik, E. R. Savinova, S. Weinkauf and U. Stimming, *Phys. Chem. Chem. Phys.*, 2005, **7**, 385–393.
47 S. Pang, W. Io and J. Hao, *Adv. Sci.*, 2021, **8**, 2102207.